Hyperspectral Optical, Thermal, and Microwave L-Band Observations For Soil Moisture Retrieval at Very High Spatial Resolution

Nilda Sánchez, Maria Piles, José Martínez-Fernández, Mercè Vall-llossera, Luca Pipia, Adriano Camps, Albert Aguasca, Fernando Pérez-Aragüés, and Carlos M. Herrero-Jiménez

Abstract

The results of an experiment conducted in Spain over the Soil Moisture Measurement Stations Network of the University of Salamanca (REMEDHUS) are presented. The observations included airborne observations from hyperspectral optical, thermal, and microwave sensors coinciding with intensive field measurements. The hyperspectral optical and thermal datasets were first analyzed and processed to select the best hyperspectral features to be included in the soil moisture retrieval procedure. A linear model linking the selected hyperspectral features to the microwave observations and the in situ soil moisture is proposed. The application of this model resulted in soil moisture estimates that agree with in situ measurements (correlation coefficient: R >0.76, root mean squared differences: RMSD <0.07 m^3m^{-3}). The hyperspectral dataset strengthened the link between optical, thermal and microwave L-band observations with soil moisture, and provided a spatial framework to disaggregate soil moisture at very high spatial resolution (3.5 m), useful in hydrological modeling and precision agriculture.

Introduction

The first two space missions dedicated specifically to soil moisture retrieval from passive L-band observations are leading to intense scientific activity. The European Spatial Agency (ESA) Soil Moisture and Ocean Salinity (SMOS) mission (Kerr *et al.*, 2010) has been providing soil moisture maps since November 2009. The US National Aeronautics and Space Administration (NASA) plans to launch the SMAP (Soil Moisture Active Passive) mission in 2014; this satellite will carry a radiometer and a synthetic aperture radar on-board (Entekhabi *et al.*, 2010). Due to practical constraints on antenna size and the altitude of low Earth orbits, the spatial resolution of SMOS and SMAP radiometers is limited to 40 to 50 km. This resolution is adequate for many global applications but restricts the use of the resulting data in regional studies over land, where a resolution of 1 to10 km is needed (Crow *et al.*, 2000; Entekhabi *et al.*, 1999; Piles *et al.*, 2011). Multi-sensor disaggregation techniques are emerging as a new technique for refining broad resolution observations using a variety of optical sensors. Combining optical and microwave data, some studies have shown that soil moisture estimates can be obtained at intermediate spatial resolutions that compare well with *in situ* data. Visible/infrared/thermal sensors are used to provide indirect measurements of soil moisture at high resolution; these measurements are combined with accurate passive microwave observations to construct soil moisture maps with resolutions ranging from several tens of meters with 15 day revisit (Merlin *et al.*, 2013) to 1 km daily (Kim and Hogue, 2012; Merlin *et al.*, 2005; Piles *et al.*, 2011). Microwave/optical data merging methods for estimating high resolution soil moisture are generally based on the intrinsic relationship between vegetation indices (VI) and land surface temperature (LST) with soil moisture using empirical approaches (Carlson *et al.*, 1994; Price, 1990; Sobrino *et al.*, 2012). This relationship can be graphically represented by a triangular-trapezoidal shape, which is formed by the scatter plot of surface temperature versus. vegetation indices under a full range of vegetation covers and soil moisture availability (Tang *et al.*, 2010). The so-called surface temperature-vegetation index (LST-VI) triangle method was first introduced during the 1990s by Price (1990) and later elaborated upon by Carlson *et al.* (1994 and 1995). It has been frequently used to estimate evapotranspiration or evaporative fraction (Batra *et al.*, 2006; Jiang and Islam, 2001; Moran *et al.*, 1994; Venturini *et al.*, 2004), determine soil moisture (Gillies *et al.*, 1997; Sandholt *et al.*, 2002) and downscale coarse-scale microwave soil moisture estimates (Chauhan *et al.*, 2003; Kim and Hogue, 2012; Piles *et al.*, 2011). In Piles *et al.* (2011), a regression analysis was performed relating soil moisture reference data (SMOS L2 product) to MODIS LST, MODIS Normalized Difference Vegetation Index (NDVI) and SMOS L1 brightness temperatures (BT). The objective was to develop a robust model to link 40-km SMOS and 1-km MODIS observations to soil moisture and to generate a SMOS-L4 soil moisture product as an optimal blend of microwave/visible data at 1 km resolution. In the present study, the objective is to improve upon this research line by using simultaneous hyperspectral and L-band airborne imagery.

Hyperspectral sensors have been used primarily to indirectly estimate soil moisture, but the best spectral range for detecting soil moisture has yet to be determined. Aside from the microwave range, visible near-infrared (VNIR) (0.4–1.4 µm), near-infrared (NIR) (0.75–1.4 µm), short-wavelength infrared (SWIR) (1.4–3.0 µm), and thermal infrared (TIR)

Nilda Sánchez, José Martínez-Fernández, and Carlos M. Herrero-Jiménez are with the Universidad de Salamanca, CIALE, Duero 12, 37185 Salamanca, Spain (nilda@usal.es).

Maria Piles, Mercè Vall-llossera, Adriano Camps, and Albert Aguasca are with the Universitat Politècnica de Catalunya, Jordi Girona 1-3, E-08034 Barcelona, Spain.

Luca Pipia and Fernando Pérez-Aragüés are with the Programa Català d'Observació de la Terra-Institut Cartogràfic de Catalunya (PCOT/ICC), Parc de Montjuïc, Barcelona, 08038, Spain.

Photogrammetric Engineering & Remote Sensing
Vol. 80, No. 8, August 2014, pp. 745–755.
0099-1112/14/8008–745

doi: 10.14358/PERS.80.8.745

(3.5–20 μm) have shown promising results (Finn *et al.*, 2011). Remotely sensed indices in the VNIR range have been compared against *in situ* observations (Adegoke and Carleton, 2002; Schnur *et al.*, 2010; Wang *et al.*, 2007) and modeled soil moisture (Farrar *et al.*, 1994), although there is evidence that the SWIR region is better suited for measuring soil water content (Lobell and Asner, 2002; Whiting *et al.*, 2004). As an alternative to broad-band multispectral remote sensing sensors, which cover relatively wide ranges of the electromagnetic spectrum, hyperspectral sensors collect images with high spectral resolution (Finn *et al.*, 2011).

However, remote sensing observations of soil moisture average within-pixel variability, thereby masking the underlying heterogeneity observed at the land surface. The ability of hyperspectral data to significantly improve the characterization, discrimination, modeling, and mapping of crops and vegetation in comparison to broadband multispectral remote sensing is well known (Thenkabail *et al.*, 2011). Currently, little research has investigated the potential of combining microwave BT and hyperspectral solar reflectance; the present work proposed the use of hyperspectral observations from the Compact Airborne Spectrographic Imager (CASI 550). The ultimate goal of the airborne experiment over the Soil Moisture Measurement Stations Network (REMEDHUS) of the University of Salamanca was to explore the potential of using CASI hyperspectral features combined with BT and land surface temperature to obtain fine-scale soil moisture estimations. First, analysis and selection of the hyperspectral dataset are required. When working with a wide number of hyperspectral bands, no single best approach is available to determine the optimal number of bands that will provide the best estimates of vegetation characteristics (Thenkabail *et al.*, 2004). Feature selection reduces the dimensionality of the data by selecting only a subset of the measured features to act as predictor variables. Large data volumes can be reduced through several data mining methods, such as projection based methods (principal or independent component analysis), similarity or divergence measures, lambda versus lambda R^2 models, and hyperspectral indices (Thenkabail *et al.*, 2013). The optimal information required to quantify crop characteristics may be captured with a relatively small number of specific narrowbands (Thenkabail, 2011). Here, the targeted vegetation characteristics should be related to the soil moisture condition; therefore, the preliminary objective was to determine whether consistent differences occurred in the VNIR spectral response between common land uses, specifically in regard to their differentiated soil moisture content.

The specific objectives of this study are as follows: (a) to determine the optimal vegetation descriptor from the hyperspectral imagery through analyzing and processing individual narrow wavebands, ratios of reflectance bands, and derivatives of reflectance spectra, and (b) to evaluate the joint use of hyperspectral products, thermal observations, and L-band data to estimate soil moisture. With the latter aim, the polynomial-fitting model proposed in Piles *et al.* (2011) for downscaling SMOS soil moisture estimates is tested, and the results are compared at very high resolution with *in situ* measurements.

Dataset

Study Area and Field Campaign

The study area is located within a 1,300 km^2 area (41.1° to 41.5°N; 5.1° to 5.7°W) in a central semiarid sector of the Duero basin, Spain (Figure 1), where the REMEDHUS network (Sánchez *et al.*, 2012) is providing soil moisture data since 1999. The climate in this region is a continental semi-arid Mediterranean with a pronounced seasonality typical of the Mediterranean climate. For example, the summer, the season in which the experiment took place, is hot and dry. The area is relatively flat but has a gentle slope, with the altitude declining towards the northeast, where the Duero River is located (Figure 1). A detailed description of the area and the REMEDHUS equipment can be found in Sánchez *et al.* (2010).

Soil moisture measurements were acquired at 0 to 5 cm depth using Theta Probe sensors (Type ML2x, Delta-T Devices) at 47 test locations during the flight duration. Four random measurements were acquired at each location within an area of 1 m^2 and geolocated in the field using a differential Global Positioning System instrument. Surface soil temperature was also measured with an infrared thermometer. All the ground measurements were taken with the aim of reflecting different soil moisture conditions in the area; the plots were large enough to surpass the spatial resolution of the broader sensor, i.e., 60 m × 60 m. Additionally, the test sites were selected to cover the different agricultural land uses in the area, including rainfed and irrigated herbaceous crops during this period (Table 1).

TABLE 1. CHARACTERISTICS OF THE FIELD PLOTS

Land use	Crop/type	Growing stage	Soil texture	# of Samples
Rainfed	Cereals	Harvesting/stubble	Sandy loam/ loamy sand	29
	Sunflower	Seed development	Sandy loam/ loamy sand	9
	Vineyard	Setting fruits	Sand	5
Fallow	Bare soil		Sandy loam/ loamy sand	7
Irrigated	Cereals	Setting grains	Sandy loam	6
	Sugar beet	Leaf development	Sandy loam	4
	Sunflower	Seed development	Sandy loam	3

In addition, data from 16 permanent stations of the REMEDHUS network were used. Hence, a total of 63 point measurements of *in situ* soil moisture were collected. One half of the samples were used to establish the coefficients of the regression in the linking model (training subsample). The other half of the samples (validating subsample) were used to validate the soil moisture maps obtained after applying the linking model.

Flight and Airborne Sensors

The flight took place on 04 July 2012. Airborne hyperspectral observations were acquired with two sensors owned by the Institut Cartogràfic de Catalunya (ICC): the Thermal Airborne Spectrographic Imager (TASI 600) and the Compact Airborne Spectrographic Imager (CASI 550). Radiometric data was acquired by the Airborne RadIomEter at L-band (ARIEL-2), which was provided by the Universitat Politècnica de Catalunya. The characteristics of the sensors are summarized in Table 2. Sensors were on-board the ICC Cessna 208 Caravan and the acquisitions spanned between 06:30 and 09:45 AM (UTC). Thirteen strips were captured to cover the study area with a lateral overlap of 40 percent (Figure 1). The flight height (which depends on the cross-track spatial resolution required) and the number of bands acquired (which depends on the along-track pixel dimension and the frame rate) were adjusted to achieve a ground spatial resolution of 3.5 m, resulting in a flight height of 3,022 m, 72 bands for CASI, and 32 bands for TASI. Weather conditions were optimal with clear sky and moderate wind.

CASI 550

The CASI 550 is a VNIR pushbroom sensor working in the spectral range of 400–1000 nm, with up to 288 programmable bands and a spectral resolution of 2.2 nm. In this project, 72 bands were acquired, covering the region from 406 nm to 957 nm. Images were acquired as 14-bit digital values at and converted into 16-bit radiances. Geometric correction was applied with a

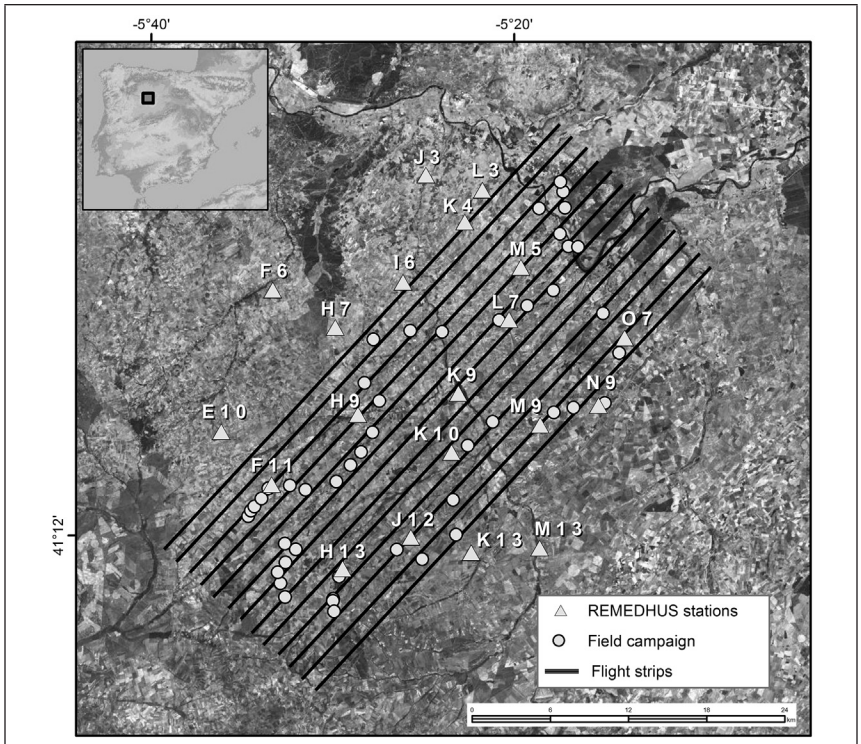

Figure 1. Flight strips and locations of the *in situ* soil moisture measurements.

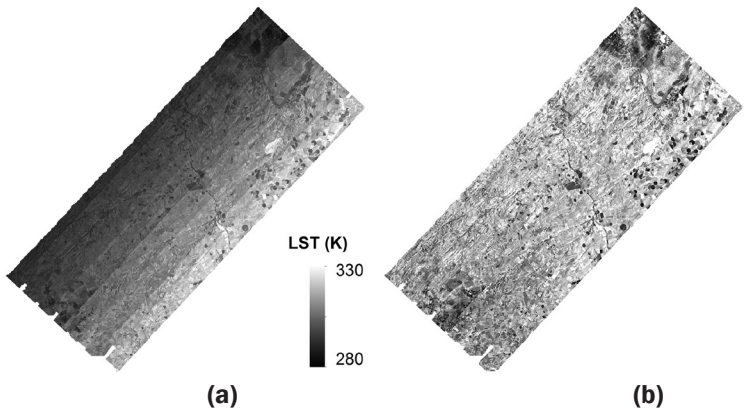

Figure 2. Images of LST (a) before, and (b) after the radiometric normalization.

TABLE 2. CHARACTERISTICS OF THE SENSORS USED IN THE DATA COLLECTION

	Spectral range	Bandwidth	# of Bands	Radiometric resolution	FOV	Spatial resolution
CASI 550	406 to 957 nm	2.2 nm	72	14 bits	40.4°	3.5 m
TASI 600	8 to 11.5 µm	110 nm	32	14 bits	40º	3.5 m
ARIEL-2	1.413 GHz	10 MHz	1	14 bits	25º	60 m

digital elevation model and ground control points. Atmospheric correction was also applied to retrieve a reflectivity profile at the pixel level using the 6s code (Vermote *et al.*, 1997) and standard values for the continental-atmospheric model.

TASI 600

The TASI 600 sensor is a pushbroom hyperspectral thermal sensor configured for this work with 32 channels operating in the 8 to 11.5 µm range. As with the CASI 550 observations, radiometric calibration and geometric correction were applied. Atmospheric thermal contributions were corrected using local temperature and relative humidity profiles provided by the National Centres for Environmental Prediction (NCEP) and the ModTRAN5.0 code. Finally, absolute temperature information was retrieved using the Temperature and Emissivity Separation (TES) technique tailored to TASI spectral properties (Pipia *et al.*, 2010). In this campaign, airborne observations were continuously acquired during the 3 hour-15 minute flight duration. Hence, a marked temperature gradient, approximately 10K, was induced by the increasing solar radiation between the first strips acquired and the last ones, as shown in Figure 2. This gradient might yield unreasonable values of soil moisture; thus, a relative radiometric normalization was proposed, using the central strip as the baseline to tie the rest of strips. This procedure balances the LST observed during the entire flight and allows the application of the mosaic of

temperatures to be applied to the linking model (Figure 2). Nevertheless, the linking model was tested both with and without this pre-treatment, and the results were compared.

ARIEL-2

The L-band radiometer (ARIEL-2) has a seven patch antenna array designed to be fitted in the aircraft photogrammetric windows ($\varnothing$ = 50 cm), with a half power beamwidth (HPBW) of 25° and a radiometric accuracy of 1K. ARIEL-2 is the second version of the ARIEL-1 radiometer prototype (Acevo-Herrera *et al.*, 2010) developed for small remote controlled aircrafts, and it includes an internal cold load for improved calibration. It has a single nadir-looking beam and a single polarization (horizontal). The spatial resolution of the observations is flight-height dependent. For convenience, in this study ARIEL-2 observations have been resampled to a 60-m regular grid.

Methods

Hyperspectral CASI Processing and Selection

The processing of hyperspectral bands in this work was not designed to determine the optimal number of bands required to discriminate crop species (which is a standard preprocessing of hyperspectral datasets) but rather to detect which bands behave in a different manner depending on the different soil moisture content of each sample. Spectral curves were obtained from every CASI band for each field plot. Bands affected by systematic errors, spectral inconsistencies and/or atmospheric absorption (Thenkabail *et al.*, 2004) were detected and removed. At the time of the experiment, the soil moisture content differed greatly among land uses; therefore, the mean spectrum of each crop was plotted separately by land uses (Table 1). The average soil moisture content was also indicated. The aim of qualitatively comparing these plots was to detect possible differences in spectral curves related to soil moisture.

For a quantitative analysis, the lambda versus lambda R^2 model (Thenkabail *et al.*, 2004, 2011, and 2013) was applied to provide a rigorous search criterion or data-mining technique to highlight wavebands with unique information content. For each sample, every single CASI waveband was correlated with every other waveband, leading to lambda versus lambda plots. A very high value of R^2 between any two wavebands indicated similar or redundant information. The areas of lowest correlation between wavebands indicated that the two bands contained unique information. Because the samples were clustered and plotted by land uses (which in turn influenced the soil moisture content), the comparison between the R^2 plots provided quantitative information for discriminating the best bands to be compared for the soil moisture estimation. In other words, the objective was to find which CASI bands were most affected by the different soil moisture contents observed in the samples. Once selected, these bands will be assessed as vegetation proxies in the soil moisture linking model, in the form of isolated bands, derivatives or combinations of them.

Hyperspectral Features versus Soil Moisture

The applicability of the hyperspectral bands to the direct estimation of soil moisture was also assessed. The correlations between soil moisture and reflectance in individual narrow frequency bands, derivatives of bands and hyperspectral indices were calculated. Previous studies have correlated soil moisture content to hyperspectral observations in the VNIR region, either by comparison with the simple bands, derivatives, indices or ratios; by analysis of principal components; or by another approach (Bach and Mauser, 1994; Ben-Dor *et al.*, 2002; Kaleita *et al.*, 2005; Wang *et al.*, 2011); most of these studies were conducted in laboratory conditions. Although some of these studies have shown that VNIR spectra can be used to produce quantitative soil moisture surface maps, quantification of soil moisture using these wavelengths remains difficult because other soil chemical and physical properties and vegetation cover also exhibit significant variability; it is difficult to decouple these effects (Lobell and Asner, 2002).

A preliminary analysis was performed, comparing each CASI hyperspectral band with the soil moisture data collected at the 63 measurement points. The statistical correlation of each CASI band with the soil moisture ground measurements was investigated.

It has been suggested in the literature that spectral derivatives have important advantages over spectral reflectance, such as their ability to reduce variability from changes in illumination or soil/litter reflectance (Blackburn, 2004) and their feasibility of defining the wavelength position of the red edge. The relationship of the first and second derivatives of the reflectance spectra with soil moisture has also been investigated.

Ratios of CASI reflectance in narrow bands were also tested. The indices used in this study were the Normalized Difference Vegetation Index (NDVI; Equation 1) (Gamon *et al.*, 1992; Rouse *et al.*, 1974), normalized differences in the red-edge region (Equations 2, 3, and 4) (Vogelmann *et al.*, 1993), the Modified Triangular Vegetation Index (MTVI; Equation 5) (Haboudane *et al.*, 2004), and the Transformed CARI (C_{ab} Absorption in Reflectance Index, TCARI, Equation 6) (Haboudane *et al.*, 2002). These indices are common in the literature, but their selection was based upon the regions of the reflectance curve that showed distinctive responses in the comparison of wet and dry samples from the previous analysis of lambda by lambda R^2:

$$\text{NDVI} = (R_{774} - R_{677})/(R_{774} + R_{677}) \quad (1)$$

$$\text{Red Edge} = (R_{734} - R_{747})/ (R_{715} + R_{726}) \quad (2)$$

$$\text{Red Edge 1} = (R_{725} - R_{712})/ (R_{725} + R_{712}) \quad (3)$$

$$\text{Red Edge 2} = (R_{734} - R_{720})/ (R_{734} + R_{720}) \quad (4)$$

$$\text{MTVI} = 1.2[(1.2(R_{800} - R_{550}) - 2.5(R_{670} - R_{550})] \quad (5)$$

$$\text{TCARI} = 3[(R_{700} - R_{670}) - 0.2(R_{700} - R_{550})/(R_{700}/R_{670})]. \quad (6)$$

The objective of this analysis was twofold. In addition to the study of the direct relationship of CASI reflectance with soil moisture, this analysis aimed to find the best hyperspectral descriptor of soil moisture to be included in the proposed linear linking model to improve the accuracy of soil moisture estimates.

The NDVI-LST 2D Space and the Proposed Model

The triangle-trapezoid method is based on the scatter plot of LST and NDVI in two-dimensional space. The resulting figure shows that the pixels for a specific area and date typically form a triangle or trapezoid in which a "wet" edge and a "dry" edge along the boundaries can be determined (Kim and Hogue, 2012). The premise of the triangle method is that LST is sensitive to soil moisture content and vegetation cover (Kim and Hogue, 2012). Identification of the triangular shape in the pixel distribution requires a flat surface and a large number of pixels over an area with a wide range of soil wetness and fractional vegetation cover (Carlson, 2007).

Soil moisture downscaling algorithms have been developed based on the unique relationship between soil moisture, NDVI, and LST for a given region under specific climatic conditions and land surface types (Chauhan *et al.*, 2003; Kim and Hogue, 2012; Piles *et al.*, 2011). This relationship can be expressed through a regression formula that links soil moisture to vegetation descriptors (such as NDVI or other indices or derivatives) and LST, as follows (Equation 7):

$$SM = \sum_{i=0}^{n}\sum_{j=0}^{n} a_{ij} NDVI^{*i}\, LSY^{*j} \quad (7)$$

where SM is soil moisture, a_{ij} are the coefficients of the polynomial relationship, and the subscripts i and j pertain

to NDVI* and LST*, which are the scaled values between the minimum and maximum NDVI and LST, respectively (Equations 8 and 9). For NDVI, minimum correspond to bare soil and maximum to vegetation cover close to 100 percent:

$$NDVI^* = (NDVI - NDVI_{min})/(NDVI_{max} - NDVI_{min}) \quad (8)$$

$$LST^* = (LST - LST_{min})/(LST_{max} - LST_{min}) \quad (9)$$

Chauhan *et al.* (2003) added the surface albedo to the right side of Equation 7 to strengthen the relationship and expanded it to the second order polynomial. Piles *et al.* (2011) proposed a downscaling algorithm for SMOS built upon this schema and showed that adding BT to Equation 7 was necessary to capture soil moisture variability at 1 to 10 km spatial resolution. This addition strengthens the weight of the radiometer high sensitivity to soil moisture content (Schmugge *et al.*, 2002), while keeping the spatial detail of the VNIR information in the model. Note that the relationship between BT at L band and the surface soil moisture is the basis of the passive missions dedicated to surface soil moisture retrievals, such as SMOS and SMAP.

In this study we explored the synergies of TASI-derived LST, different CASI-derived vegetation indices, ARIEL brightness temperatures and *in situ* soil moisture using the following linear linking model, which is a simplification of the one proposed in Piles *et al.* (2011):

$$SM = a_0 + a_1 VI^* + a_2 LST^* + a_3 BT^* \quad (10)$$

where SM is the estimated soil moisture, a_0 is a standalone coefficient, and a_1, a_2, and a_3 are the coefficients of VI*, LST* and BT*, respectively. A system of linear equations was set up for the pixels of the *in situ* training subsample using Equation 10. The value of each point measurement was extracted from each image at its original resolution (3.5 m for CASI and TASI, 60 m for ARIEL). The training subsample was selected as being representative of the different land uses. Note that the subsample selection within each land use did not affect the coefficient determination (not shown). The system was solved to obtain the regression coefficients: a_0, a_1, a_2, and a_3. The hyperspectral features that were best correlated to soil moisture in the former analysis were tested as an alternative to NDVI in the model. Metrics of the regression (the determination coefficient, R^2; the root mean square error, RMSE; and the p-value at 95 percent confidence level) were used to evaluate the performance of the linking model.

Once the linking model was set up, it was applied to CASI, TASI, and ARIEL imagery, and the results were compared with the validating subsample. The metrics applied were the bias, the standard deviation, the root mean square difference (RMSD) and the correlation coefficient (R) with a p-value at the 95 percent confidence level. These are the metrics typically used to predefine the accuracy requirements of a satellite's soil moisture product (Kerr, 2007; Loew and Schlenz, 2011; Sánchez *et al.*, 2012). The R (Pearson) value was used as an indicator of the strength and direction of the comparisons, and R^2 was used to describe how well the soil moisture can be predicted by a multiple regression approach.

Results and Discussion

Hyperspectral and Lambda versus Lambda R^2 CASI Analysis

The analysis of the spectral curves detected two wavelength portions of the spectra (754.5 to 762.18 nm and 925.9 to 948.83 nm) affected by atmospheric absorption, corresponding to CASI bands (47 to 48 and 69 to 70 to 71, respectively). Hence, the data in these bands were removed from the analysis. The last band (72) was also removed to avoid isolated data. Accordingly, a total of 68 bands were used in the analysis.

Hyperspectral curves were plotted, corresponding to specific species involving land uses, i.e., irrigated crops (Figure 3a), rainfed crops (Figure 3b), and fallow (Figure 3c). When the data were analyzed, the mean spectral curve from plots with the same crop was used.

After a simple visual analysis, some qualitative differences in the spectral curves related to the soil moisture can be distinguished. The typical well-watered vegetation curve corresponded to the irrigated crops (Figure 3a), where a high reflectance in the near-infrared area and a low reflection in the red region are noteworthy; this pattern is most pronounced for the sugar beet crop. On the contrary, the rainfed crops curve (Figure 3b), which is similar to that of the bare soil (fallow, Figure 3c), increases slightly from the visible to the infrared. The increase is more pronounced for cereals than for the other rainfed crops, as the cereal plots were harvested prior to the data collection, and it can be assumed that this crop behaves as bare soil (Figure 3c). The rest of the rainfed crops with vegetation activity (vineyards and sunflowers) showed patterns similar to bare soil; the sparse coverage of these plants and their limited activity due to water scarcity contribute to a signal similar to the soil spectral response. The different spectral responses for the same crop under rainfed/irrigated conditions are notable in Figures 3a and 3b for sunflowers.

The soil irrigation status more affected the shape of the curve than the reflectance quantities, notably in the visible region. Identifying the precise regions where the changes took place was the aim of the lambda versus lambda correlation analysis, following the model of Thenkabail *et al.* (2004 and 2013). Lambda versus lambda plotted areas with the least R^2 values for two wavebands were the areas with the highest information content (Thenkabail *et al.*, 2004). For this study, a 68 × 68 band-correlation matrix was developed, and the correlation was converted to R^2. This dataset provided 4,624 coefficients involving all possible combination of wavebands, which were represented as a raster plots (Figure 4). The R^2

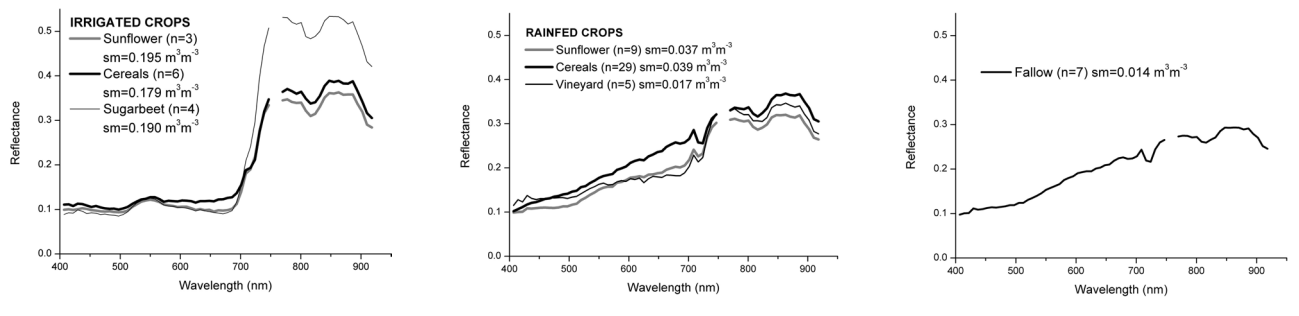

Figure 3. Mean spectral profiles of hyperspectral datasets for crop species and land uses in the study area: (a) irrigated crops (b) rainfed crops, and (c) fallow areas.

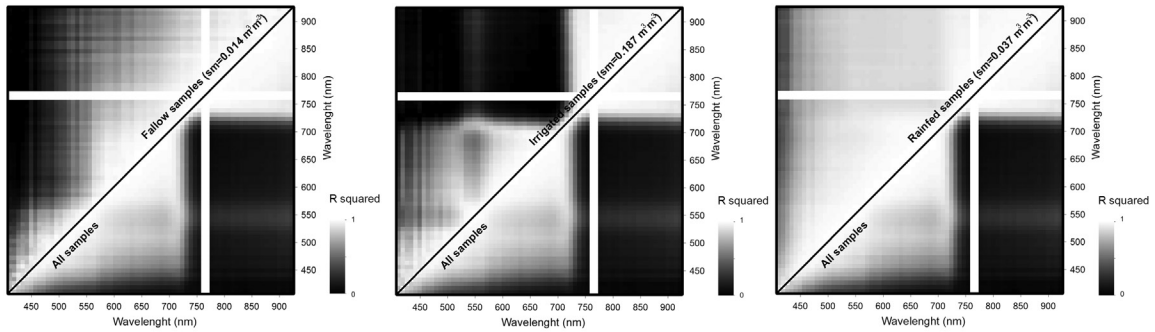

Figure 4. Lambda versus lambda R^2 plots. The areas with the lowest R^2 (in black) are the waveband regions with the highest information content. The plots include all crop species (below the diagonal) and (a) irrigated crop species, (b) rainfed crops, and (c) fallow areas above the diagonal.

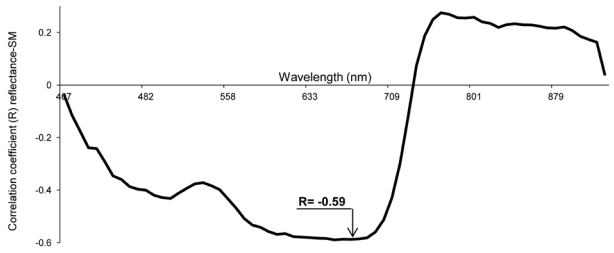

Figure 5. Correlation between *in situ* soil moisture and reflectance by wavelength.

TABLE 3. CORRELATION COEFFICIENT (R) OF *IN SITU* SOIL MOISTURE (63 SAMPLES) WITH THE HYPERSPECTRAL INDICES, THE REFLECTANCE BANDS AND THE FIRST DERIVATIVES OF REFLECTANCE SPECTRA; ALL CORRELATIONS WERE STATISTICALLY SIGNIFICANT AT A 95 PERCENT CONFIDENCE LEVEL

	R
NDVI	0.77
Red Edge	-0.75
Red Edge 1	0.76
Red Edge 2	0.80
MTVI	0.72
TCARI	0.69
First derivative, 701 to 709 nm	0.56
First derivative, 716 to 724 nm	0.69
First derivative, 731 to 739 nm	0.62
Band 656 to 663 nm	0.59

values for all the samples were plotted just below the diagonal of the matrix (2,312 coefficients), as values on either side of the diagonal were the transpose of one another. Above the diagonal, the coefficients for irrigated, rainfed and fallow samples are shown in three plots (Figure 4a, 4b, and 4c).

These plots, together with the quantitative analysis of R^2, provided the wavebands with the least redundancy and identified those that best model the vegetation spectra response to the soil moisture. The strength of the hyperspectral data is best tested by plotting lambda versus lambda plots within a single land use (e.g., different rainfed crops), where spectral similarities are likely to be close. The cross-correlations between different plant species or land uses do not test the strength of hyperspectral data since these categories already have very distinct spectra (Figure 3) (Thenkabail *et al.*, 2004). In this case, the most differentiated pairs of bands are not the same for rainfed and irrigated plots because of the different growing conditions related to their water availability. Thus, the lambda versus lambda R^2 not only provides the best combination for each land use but also indicates the differences among each land use, which is expected to be related to different soil moisture contents.

Taking a threshold of R^2 <0.03 for paired bands, the regions containing unique information (the least redundancy) for each land use are extracted (the table containing all R^2 values is not presented). For irrigated crops, the best spectral region combinations spanned between the region from 406 to 505 nm versus the region from 724 to 926 nm and the region from 620 to 678 nm versus the region from 731 to 926 nm. For the fallow samples, the best combinations were the region from 406 to 437 nm versus the region from 610 to 926 nm. For rainfed samples, any pairwise combination of bands afforded an R^2 below this limit. Thus, since both irrigated and fallow samples coincided for the regions with least correlations in the range between ~400 to ~500 nm versus ~700 to ~900 nm, a definite and useful pair of hyperspectral bands were recommended, comparing the 620–678 nm region (Bands 29 to 37) with the 730–926 nm region (Bands 44 to 68) of CASI. These bands stressed the differences between soil moisture contents and provided non-redundant information at the same time.

Hyperspectral Bands, First Derivatives and Indices as Proxies of Soil Moisture

The correlation values of each CASI band with soil moisture measurements (Figure 5) show a shape that coincides with the typical reflectance curve of a vegetated area. This result could be related to the fact that, for this date, higher soil moisture content corresponds to higher NIR reflectance from the irrigated crops, leading to a positive correlation in this region (770 to 880 nm). Conversely, the very low soil moisture content corresponds to bare soils or soils without vegetation activity (stubble), with typically high reflectance in the red region (650 to 700 nm). For this reason, the correlation of the reflectance spectra with soil moisture is negative in the red region. The strongest correlation was observed in the 650 nm to 700 nm region, with a maximum negative correlation coefficient of –0.59 located between the red and red-edge region (Figure 5). In those regions, the higher reflectance occurred for the surfaces of bare soil, which were dry during data collection (beginning of July). Furthermore, the negative value of R expresses a decrease in the reflectance with increasing soil moisture, which is a known effect over the visible to SWIR range (Haubrock *et al.*, 2008).

The tests of the first derivatives of CASI reflectance spectra show different responses to soil moisture contents in the 701 to 709 nm, 716 to 724 nm, and 731 to 739 nm bands, all of which are in the region of the red edge (Table 3). The amplitudes of the second derivatives did not have a significant correlation to soil moisture; thus, this analysis was discarded.

The hyperspectral indices based on the reflectance at the red-edge and the NIR bands had a better correlation to soil moisture than the visible-based bands did. Any band or first derivative separately showed a better correlation than the

hyperspectral indices (Table 3). NDVI and Red Edges 1 and 2 were the indices with the best correlations and, therefore, the indices that have been included as alternatives in the linking model calculation. Nevertheless, further analysis should be performed to find the optimal hyperspectral vegetation indices by computing the normalized ratios from every possible two-band combination of CASI bands and correlating them with soil moisture. This procedure for extracting the best indices (Thenkabail, 2013) is similar to the lambda versus lambda analysis for all bands.

Because BT was added to the linking model, its performance for estimating soil moisture separately was also tested using the same procedure as for bands, derivatives and indices. A correlation coefficient of –0.60 was obtained between BT and soil moisture, a worse result than most of the hyperspectral features compared with soil moisture (Table 3). The correlation between soil moisture and LST resulted in a non-significant correlation of –0.36, showing a weak relationship. We hypothesize that coupling hyperspectral features, LST and BT, could improve the estimation of soil moisture compared to using a unique estimator.

Performance of the Universal Triangle

Figure 6 represents a scatter plot including all the image pixels in the NDVI-LST space. Soil moisture conditions vary from high values on the bottom of the image to low values on the top. The dry edge is represented by the top limit of the cloud point, which expresses the limit of water stressed conditions and warmer pixels, and the bottom limit shows the wet edge and colder pixels. The polygon's edges can be interpreted as the minimum/maximum reached by vegetation cover (NDVI) and soil moisture (Piles *et al.*, 2011).

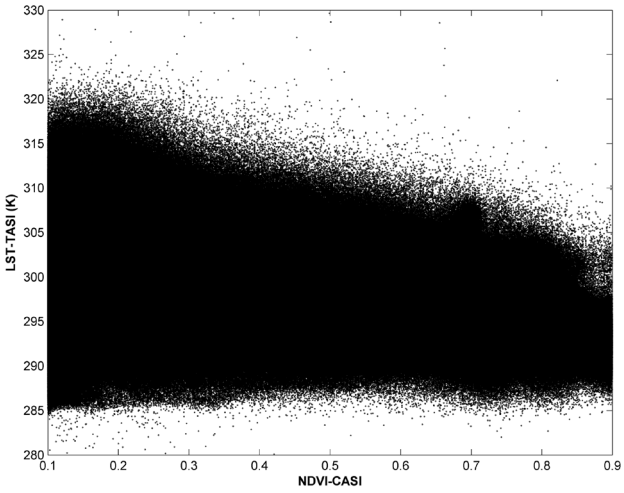

Figure 6. Scatter plot of pixel values of NDVI-CASI versus LST-TASI from the image taken in the REMEDHUS area during the flight on 04 July 2012. The dry/warm edge is evident from the sharply defined top side of the pixel envelope.

The scatter plot generated from aircraft measurements using the CASI and TASI sensors at high spatial resolution shows better-defined edges than the plot using broader resolution imagery. As stated by Carlson (2007), the triangle method is effective with higher resolution imagery such as that from Landsat or aircraft radiometers because the triangle is more easily resolved.

Figure 7 shows a subzone of the NDVI and LST images of the study area containing irrigated and rainfed crops and the associated scatter plot between NDVI-CASI and LST-TASI. The highest NDVI in Figure 7a corresponded to the irrigated areas, which in turn showed the lowest LST (Figure 7b). On the contrary, rainfed and stubble-covered areas corresponded to lower NDVI and higher LST. These two soil uses can be separately distinguished in the NDVI-LST scatter plot (Figure 7c). The cluster of the top-left area of the plot corresponds to the drier rainfed areas, whereas the bottom-right cluster

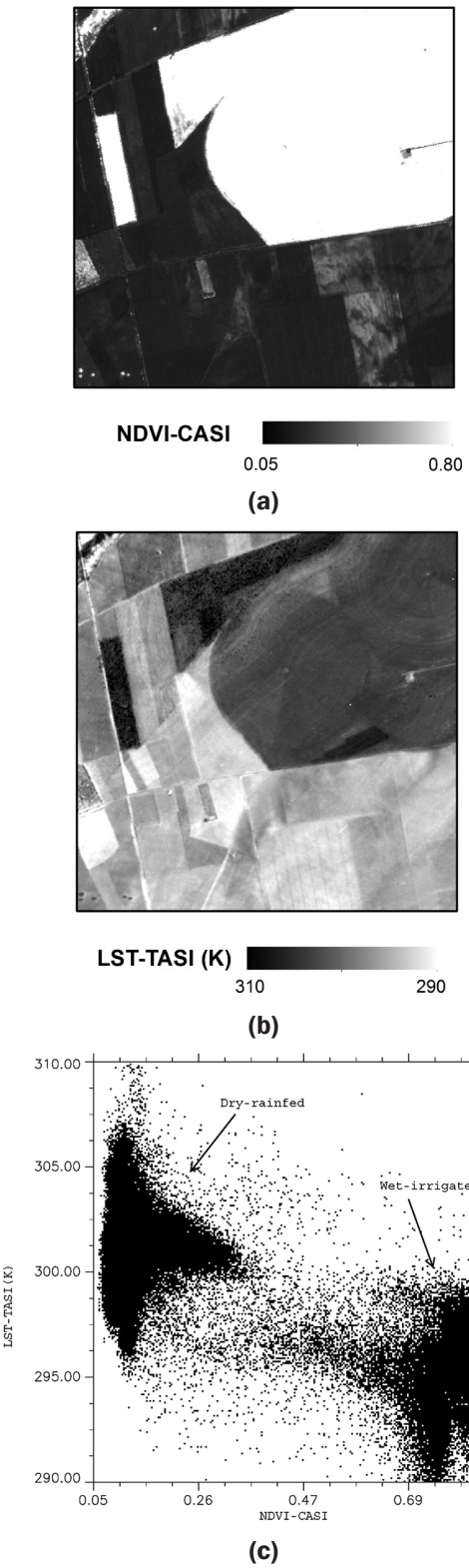

Figure 7. (a) NDVI-CASI image, (b), LST-TASI image, and (c), scatter plot of the area where the irrigated and rainfed crops are separately distributed.

corresponds to the wetter irrigated plots. The link between the scatter plot and the imagery confirmed the potential of the NDVI-LST 2D space for separating the soil moisture content associated with the different land uses and agreed with the shape and the interpretation of the conceptual LST-NDVI space described in previous studies (Lambin and Ehrlich, 1996; Sandholt *et al.*, 2002). However, there was a certain variability within each category (irrigated and rainfed) in the NDVI-LST scatter plot (Figure 7c), most likely due to factors such as crop types, soil texture, vegetation coverage, and variability in the growing states within each field, as described in Table 1.

A scatter plot containing the LST and NDVI pixels values coinciding with *in situ* observations is shown (Figure 8), in which the diameter of each point is associated with the soil moisture content. Figure 8 highlights the triangular shape of the scatter plot of the entire area in Figure 6 and the subarea in Figure 7c. The points located in the right side of the triangle, corresponding to higher NDVI and lower LST, exhibit the greatest soil moisture contents, which correspond mainly to irrigated crops, as observed in the scatter plot in Figure 7c. As expected, the available soil moisture allows for vegetation activity and results in an increase in evapotranspiration, which leads to a decrease in the surface temperature. The theoretical basis of the triangle is supported here for the very clear separation in water content between vegetated and non-vegetated areas. The irrigated crops are in their growing cycle, coinciding with a considerable water supply and high temperature, and they showed strong vegetation activity and full green coverage, which can be inferred after the analysis of the spectral curve (Figure 3a). However, non-vegetated areas such as the harvested cereals, stubble, and fallow plots had low NDVI, high LST and low soil water content. It can be stated that the soil moisture dependence on NDVI should not be considered over bare soils. Nevertheless, even for the stubble/bare soil areas, the algorithm was able to detect the low soil water content with acceptable results (R = 0.52, 0.53, and 0.53 for the NDVI and Red Edge 1 and 2 proxies, respectively), although there were no differences in land use. It is not easy to define the link between soil moisture and the vegetation proxy at the partially vegetated areas, such as the rainfed vineyards or sunflowers (Table 1). Although they had photosynthetic activity, there is no clear positive link between the canopy status (indicated by the NDVI or other indices) and water content in those soils for several reasons. On the one hand, the very low soil moisture content of these soils in the summer results in less plant development compared to the irrigated crops. On the other hand, the resolution of the observations and the scattered distribution of these plants hindered a clear separation between bare soil and green canopy. In addition, the water available for use by these plants resides in the root zone, which is a deeper layer than that the observations can penetrate (0 to 5 cm). However, the model is not only based in the NDVI response, but also in the LST, and it could be noticed that one assumption involved in downscaling algorithms based on the LST-VI triangle space is that the sensitivity of LST to soil and canopy differs and that canopy temperature is insensitive to soil moisture change at surface/deep layer (Tang *et al.*, 2010).

The model also assumes that variations in surface temperature for a given vegetation index are primarily caused by the different soil moisture availabilities rather than by differences in the atmospheric forcing (Piles et al., 2011; Tang et al., 2010). However, it has been shown that this assumption may not be valid in the TASI-derived LST without any pre-treatment. A high correlation (R^2 = 0.82) was observed between the retrieved LST and *in situ* temperature measurements (showing an accurate pre-treatment of the TASI-derived LST); however, the temperature gradient induced by the increasing solar irradiance during the flight should be compensated. An attempt to compensate for this temperature gradient during the flight duration was carried out by applying a radiometric normalization of the strips in the mosaicking process.

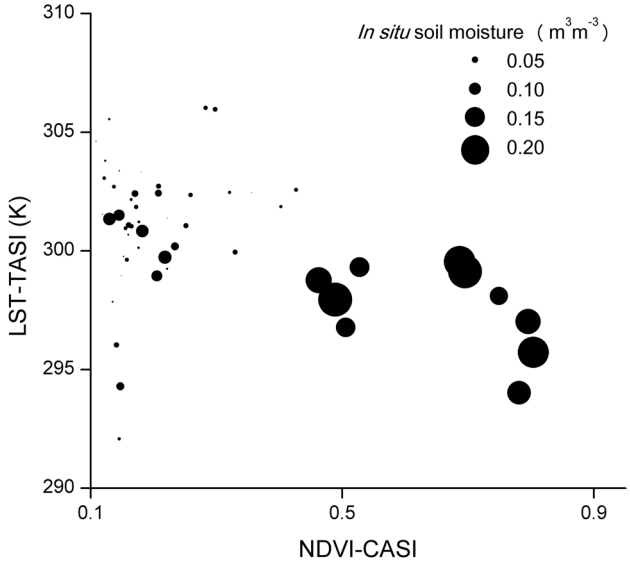

Figure 8. Scatterplot of NDVI-CASI and LST-TASI for the 63 samples used in the study. Soil moisture content is represented by the size of the circle symbols.

Linking Model

As stated before, NDVI, and Red Edges 1 and 2 were selected as vegetation proxies in the linking model. The linking model coefficients were obtained for each case; a good fit was found for each of them, with a coefficient of determination R^2 >0.72 (Table 4). Still, the RMSE obtained is below the usual target accuracy of soil moisture satellites (0.04 m^3m^{-3}) (Kerr et al., 2010; Entekhabi et al., 2010).

Table 4. Statistical Results of the Linking Model for the Three Vegetation Proxies: Coefficients of the Polynomial Fit (A_0, A_1, A_2, and A_3) with a P-value of 95 Percent, Determination Coefficient (R^2) and Root Mean Square Error (RMSE)

Model	a_0	a_1	a_2	a_3	R^2	RMSE (m^3m^{-3})
NDVI	0.09484	0.15028	–0.07375	–0.05054	0.72	0.039
p-value (95%)	0.06033	2.157E-5	0.13714	0.29183		
Red Edge 1	0.09871	0.17681	–0.06892	–0.0676	0.75	0.037
p-value (95%)	0.03485	5.30219E-6	0.14192	0.12468		
Red Edge 2	0.11127	0.19156	–0.06436	–0.08908	0.76	0.034
p-value (95%)	0.0083	7.13937E-7	0.13716	0.0262		

Because the variables in the linking model are normalized, the associated coefficients indicate the importance that each variable plays in the linking model. According to these results, the best soil moisture predictors are the hyperspectral ratios, particularly the Red Edge 2, because a_1 is the highest coefficient. LST and BT had less weight in all cases, with smaller coefficients (a_2, a_3). The negative coefficients of LST and BT indicated their inverse correlation with soil moisture, which was consistent with their separate comparison with soil moisture.

The linking model was previously trained with the values of TASI-derived LST without the proposed radiometric normalization of the LST values (Sánchez *et al.*, 2013). In that preliminary work, the same dataset and linking model were tested, but the raw values of LST were used instead of the normalized

ones. Comparing those results with the present alternative, the use of this procedure for the LST improved the results of the linking model in terms of R^2 (0.66, 0.70, and 0.75 without normalization versus 0.72, 0.75, and 0.76 with normalization) and RMSE (0.41, 0.38, and 0.35 m^3m^{-3} without normalization versus 0.39, 0.37, 0.34 m^3m^{-3} with normalization).

Validation

The three proposed linking models were applied to the CASI, TASI, and ARIEL imagery to obtain very high resolution soil moisture data at 3.5 m, and the results were compared with the validating subsample point measurements. Statistics of the comparison between estimated and observed soil moisture are reported in Table 5. The comparison showed an R >0.76 and an RMSD below or equal to 0.07 m^3m^{-3}, which could be considered very satisfactory. Moreover, the averaged bias was close to zero for the three models tested.

TABLE 5. STATISTICS OF ESTIMATED SOIL MOISTURE VERSUS *IN SITU* SOIL MOISTURE MEASUREMENTS: CORRELATION COEFFICIENT (R), MEAN DIFFERENCE (BIAS), STANDARD DEVIATION (SD), AND ROOT MEAN SQUARE DIFFERENCE (RMSD); ALL CORRELATIONS ARE STATISTICALLY SIGNIFICANT AT A 95 PERCENT CONFIDENCE LEVEL

Model	Bias (m^3m^{-3})	sd (m^3m^{-3})	RMSD (m^3m^{-3})	R
NDVI	–0.008	0.046	0.046	0.76
Red Edge 1	–0.008	0.046	0.064	0.77
Red Edge 2	–0.006	0.047	0.070	0.78

The performance of the algorithm is assessed in a fairly wide range of soil moisture conditions (0 to 0.253 m^3m^{-3}) although we are considering a single day during the dry season. Specifically, the study took place during a period in which the vegetation activity was exclusively linked with the irrigation water supply and when most of the areas (e.g., rainfed crops) behaved as bare soil because the plants had just been harvested (Table 1). This situation fits well with the theoretical basis of the universal triangle, which is based on evapotranspiration in several extreme conditions: full-cover, well-watered vegetation, full-cover vegetation with no available water, and dry bare soil (Moran *et al.*, 1994).

The fine spatial detail of the resulting estimates enhances the representativeness of the *in situ* soil moisture measurements for validating the results. In addition, ground samples have been selected to cover a wide range of conditions of soil moisture contents, which is preferable for validation purposes. Nevertheless, the temporal scale of this campaign hampers the study of seasonal changes, which can have a significant impact on soil moisture conditions.

The potential interactions between soil moisture estimates and observations at high resolution from airborne sensors allow for synergistic approaches that can be later transferred to sensors on-board satellite platforms. In this study, hyperspectral information from the visible to the infrared domain has been combined with microwave observations into an optimal blend of accurate and high spatial resolution soil moisture estimates. This approach has been tested at the *in situ* soil moisture measurement locations. The use of the proposed linking model as a downscaling approach relies on retrieving soil moisture from ARIEL's BT and solving a system of equations containing all pixels in the image. This process is beyond the scope of this paper and will be explored in the future. The comparison of the final retrieved map with a classified map from CASI is an ongoing objective, i.e., qualitatively analyzing where soils with high/low moisture are located and then quantifying the relationship by searching CASI and TASI-derived variables.

The possibility of using hyperspectral data to obtain soil moisture estimates is still uncertain but appears promising (Finn *et al.*, 2011; Grandjean *et al.*, 2010). Hyperspectral indices, particularly the Red Edges 1 and 2, have shown the capability to estimate soil moisture in the retrieval model. The NDVI provided a similar good result, and it can be argued that this index is easily retrieved from multispectral data. However, the advantage of the hyperspectral source over satellite-based data relies on its finer spatial resolution and the possibility of controlling the temporal resolution from aircraft mounted sensors (Finn *et al.*, 2011). This work shows that a hyperspectral-based airborne field experiment is able to provide soil moisture estimations with good accuracy and detailed spatial resolution. Hence, this method could replace intensive field campaigns or high-cost data collection at different spatial scales, and could be particularly promising for precision agriculture.

Conclusions

This study contributes to an on-going effort to obtain spatially accurate soil moisture data using remote sensors with different spectral ranges, which is key to progress in hydrological research and in climatic and agricultural applications. The results demonstrate the potential of using hyperspectral data in combination with thermal and microwave sensors as new inputs in the conventional soil moisture downscaling algorithms to improve the spatial resolution of passive microwave estimates. A preliminary analysis of the hyperspectral dataset is needed to avoid redundancy and to adjust the amount of data to the information needed. The result of the lambda versus lambda R^2 analysis showed that the optimal spectral regions ranged from 620 to 678 nm and 730 to 926 nm for comparison with soil moisture.

The test of the hyperspectral indices versus the soil moisture showed that indices based on the reflectance on the red-edge and NIR regions had a better correlation with in situ soil moisture (R between 0.75 and 0.80) than visible-based regions. A linear linking model was proposed to relate the three suggested vegetation indices along with LST and BT to the in situ soil moisture, showing in all cases a very good fit (R^2 >0.72). The hyperspectral bands had a better correlation with the observed soil moisture when they were integrated with LST and BT in the linking model compared to when they were used individually. The results of the model application agreed well with the in situ measurements (R >0.76 and RMSD <0.07 m^3m^{-3}).

The use of hyperspectral data can lead to significant improvements in current soil moisture downscaling algorithms based on the synergies between optical, thermal, and microwave L-band observations. Although the sensor used in this study was limited to VNIR, the additional capabilities of microwave and thermal images have shown the potential of hyperspectral data for soil moisture evaluation at very high spatial resolution. Further research must be performed with similar data under other climatic and soil moisture conditions.

Aknowledgments

The flight of this study was the result of an agreement between the Universitat Politècnica de Catalunya (UPC) and the Institut Cartogràfic de Catalunya (ICC). This study was supported by the Spanish Ministry of Science and Innovation under the projects AYA2010-22062-C05 and AYA2012-39356-C05.

References

Acevo-Herrera, R., A. Aguasca, X. Bosch-Lluis, A. Camps, J. Martínez-Fernández, N. Sánchez-Martín, and C. Pérez-Gutiérrez, 2010. Design and first results of an UAV-borne L-band radiometer for multiple monitoring purposes, *Remote Sensing*, 2:1662–1679.

Adegoke, J.O., and A.M. Carleton, 2002. Relations between soil moisture and satellite vegetation indices in the U.S. Corn Belt, *American Meteorological Society*, 3:395–405.

Bach, H., and W. Mauser, 1994. Modelling and model verification of the spectral reflectance of soils under varying moisture conditions, *Proceedings of the Geoscience and Remote Sensing Symposium*, 08-12 August, IEEE International, Pasadena, California, pp. 2354–2356.

Batra, N., S. Islam, V. Venturini, G. Bisht, and L. Jiang, 2006. Estimation and comparison of evapotranspiration from MODIS and AVHRR sensors for clear sky days over the Southern Great Plains, *Remote Sensing of Environment*, 103:1–15.

Ben-Dor, E., K. Patkin, A. Banin, and A. Karnieli, 2002. Mapping of several soil properties using DAIS-7915 hyperspectral scanner data. A case study over clayey soils in Israel, *International Journal of Remote Sensing*, 23:1043–1062.

Blackburn, G.A., 2004. Wavelet decomposition of hyperspectral reflectance data for quantifying photosynthetic pigment concentrations in vegetation, *Proceedings of the XXth ISPRS Congress; Commission 7* (O. Altan, Editor), 12-23 July 2004. ISPRS, Istanbul, Turkey, pp. 878–882.

Carlson, T., 2007. An overview of the 'triangle method' for estimating surface evapotranspiration and soil moisture from satellite imagery, *Sensors*, 7:1612–1629.

Carlson, T.N., R.R. Gillies, and E.M. Perry, 1994. A method to make use of thermal infrared temperature and NDVI measurements to infer surface soil water content and fractional vegetation cover, *Remote Sensing Reviews*, 9:161–173.

Carlson, T.N., R.R. Gillies, and T.J. Schmugge, 1995. An interpretation of methodologies for indirect measurement of soil-water content, *Agricultural and Forest Meteorology*, 77:191–205.

Crow, W., E. Wood, and R. Dubayah, 2000. Potential for downscaling soil moisture maps derived from spaceborne imaging radar data, *Journal of Geophysical Research*, 105(D2):2203–2212.

Chauhan, N., S. Miller, and P. Ardanuy, 2003. Spaceborne soil moisture estimation at high resolution: A microwave-optical/IR synergistic approach, *International Journal of Remote Sensing*, 22:4599–4622.

Entekhabi, D., G. Asrar, A. Betts, K. Beven, R. Bras, C. Duffy, T. Dunne, R.S. Koster, D. Lettenmaier, D. McLaughlin, W. Shuttleworth, M. van Genuchten, M. Wei, and E. Wood, 1999. An agenda for land surface hydrology research and a call for the second international hydrological decade, *Bulletin of the American Meteorological Society*, 80(10):2043–2058.

Entekhabi, D., E. Njoku, P.E. O'Neill, K.H. Kellogg, W.T. Crow, W.N. Edelstein, J.K. Entin, S.D. Goodman, T. Jackson, J. Johnson, J. Kimball, J.R. Piepmeier, R.D. Koster, N. Martin, K.C. McDonald, M. Moghaddam, S. Moran, R. Reichle, J.C. Shi, M.W. Spencer, S.W., Thurman, L. Tsang, and J. Van Zyl, 2010. The Soil Moisture Active Passive (SMAP) mission, *Proceedings of the IEEE*, 98(5):704–716.

Farrar, T.J., S.E. Nicholson, and A.R. Lare, 1994. The influence of soil type on the relationships between NDVI, rainfall and soil moisture in semiarid Botswana. II. NDVI response to soil moisture, *Remote Sensing of Environment*, 50:121–133.

Finn, M.P., M. Lewis, D. Bosch, M. Giraldo, K. Yamamoto, D.G. Sullivan, R. Kincaid, R. Luna, G.K., Allam, C. Kvien, and M.S. Williams, 2011. Remote sensing of soil moisture using airborne hyperspectral data, *GIScience & Remote Sensing*, 48(4):522–540.

Gamon, J.A., J. Peñuelas, and C.B. Field, 1992. A narrow-waveband spectral index that tracks diurnal changes in photosynthetic efficiency, *Remote Sensing of Environment*, 41:35–44.

Gillies, R., T.N. Carlson, J. Cui, W.P. Kustas, and K.S. Humes, 1997. A verification of the ''triangle'' method for obtaining surface soil water content and energy fluxes from remote measurements of the NDVI and surface radiant temperature, *International Journal of Remote Sensing*, 18:3145–3166.

Grandjean, G., O. Cerdan, G. Richard, I.P.L. Cousin, B. Tabbagh, B. Van Wesemael, A. Stevens, S. Lambot, and F. Carre, 2010. Digisoil: An integrated system of data collection technologies for mapping soil properties, *Proximal Soil Sensing* (R.A. Viscarra Rossel, A. McBratney, and B. Minasny, editors), Springer, New York, pp. 89–101.

Haboudane, D., J.R. Miller, E. Pattey, P.J. Zarco-Tejada, and I.B. Strachan, 2004. Hyperspectral vegetation indices and novel algorithms for predicting green LAI of crop canopies: Modeling and validation in the context of precision agriculture,*Remote Sensing of Environment*, 90:337–352.

Haboudane, D., J.R. Miller, N. Tremblay, P.J. Zarco-Tejada, and L. Dextraze, 2002. Integration of hyperspectral vegetation indices for prediction of crop chlorophyll content for application to precision agriculture, *Remote Sensing of Environment*, 81(2-3):416–426.

Haubrock, S.N., S. Chabrillat, M. Kuhnert, P. Hostert, and H. Kaufmann, 2008. Surface soil moisture quantification and validation based on hyperspectral data and field measurements, *Journal of Applied Remote Sensing*, 2(1):023552.

Jiang, L., and S. Islam, 2001. Estimation of surface evaporation map over southern Great Plains using remote sensing data, *Water Resources Research*, 37:329–340.

Kaleita, A.L., L.F. Tian, and M.C. Hirschi, 2005. Relationship between soil moisture content and soil surface reflectance, *Transactions of the American Society of Agricultural Engineers*, 48(5):1979–1986.

Kerr, Y., 2007. Soil moisture from space: Where are we?, *Hydrogeology Journal*, 15:117–120.

Kerr, Y., P. Waldteufel, J.-P. Wigneron, S. Delwart, F. Cabot, J. Boutin, M.-J. Escorihuela, J. Font, N. Reul, C. Gruhier, S.E. Juglea, M.R. Drinkwater, A. Hahne, M. Martín-Neira, and S. Mecklenburg, 2010. The SMOS Mission: New tool for monitoring key elements of the Global Water Cycle, *Proceedings of the IEEE*, 98(5):666–687.

Kim, J., and T.S. Hogue, 2012. Improving spatial soil moisture representation through integration of AMSR-E and MODIS products, *IEEE Transactions on Geoscience and Remote Sensing*, 50(2):446–460.

Lambin, E.F., and D. Ehrlich, 1996. The surface temperature-vegetation index space for land cover and land-cover change analysis, *International Journal of Remote Sensing*, 17:463–487.

Lobell, D.B., and G.P. Asner, 2002. Moisture effects on soil reflectance, *Soil Science Society of America Journal*, 66:722–727.

Loew, A., and F. Schlenz, 2011. A dynamic approach for evaluating coarse scale satellite soil moisture products, *Hydrology and Earth System Sciences*, 15:75–90.

Merlin, O., A.G. Chehbouni, Y. Kerr, E.G. Njoku, and D. Entekhabi, 2005. A combined modeling and multispectral/multiresolution remote sensing approach for disaggregation of surface soil moisture: Application to SMOS configuration, *IEEE Transactions on Geoscience and Remote Sensing*, 43(9):2036–2050.

Merlin, O., M.J. Escorihuela, M.A. Mayoral, O. Hagolle, A. Albitar, and Y. Kerr, 2013. Self-calibrated evaporation-based disaggregation of SMOS soil moisture: An evaluation study at 3 km and 100 m resolution in Catalunya, Spain, *Remote Sensing of Environment*, 130:25–38.

Moran, M.S., T.R. Clarke, Y, Inoue, and A. Vidal, 1994. Estimating crop water deficit using the relation between surface-air temperature and spectral vegetation index, *Remote Sensing of Environment*, 49:246–263.

Piles, M., A. Camps, M. Vall.llossera, I. Corbella, R. Panciera, C. Ruediger, Y. Kerr, and J. Walker, 2011. Downscaling SMOS-derived soil moisture using MODIS visible/infrared data, *IEEE Transactions on Geoscience and Remote Sensing*, 49(9):3156–3166.

Pipia, L., F. Pérez, A., Tardà, L., Martínez, V., Palà, and R. Arbiol, 2010. Thermal airborne spectrographic imager for temperature and emissivity retrieval, *Proceedings of the 3rd International Symposium on Recent Advances in Quantitative Remote Sensing (RAQRS III),* 27 September-01 October 2010, Valencia, Spain, unpaginated CD-ROM.

Price, J.C., 1990. Using spatial context in satellite data to infer regional scale evapotranspiration, *IEEE Transactions on Geoscience and Remote Sensing*, 28(5):940–948.

Rouse, J.W., R.H. Haas, J.A. Shell, D.W. Deering, and J.C. Harlan, 1974. Monitoring the vernal advancement of retrogradation of natural vegetation, Final Report, Type III, NASA/GSFC, Greenbelt, Maryland.

Sánchez, N., J. Martínez-Fernández, A Calera, E.A. Torres, and C. Pérez-Gutiérrez, 2010. Combining remote sensing and *in situ* soil moisture data for the application and validation of a distributed water balance model (HIDROMORE), *Agricultural Water Management*, 98:69–78.

Sánchez, N., J. Martínez-Fernández, A. Scaini, and C. Pérez-Gutiérrez, 2012. Validation of the SMOS L2 soil moisture data in the REMEDHUS network (Spain), *IEEE Transactions on Geoscience and Remote Sensing*, 50(5):1602–1611.

Sánchez, N., J. Martínez-Fernández, M. Piles, M. Vall-llossera, A. Camps, S. Sánchez-Ruiz, A. Gumuzzio, and C.M. Herrero-Jiménez, 2013. Soil moisture maps at very high spatial resolution through optical, thermal and L-band observations, *Proceedings of the Living Planet Symposium 2013*, European Space Agency, 09-13 September, Edinburgh, UK, unpaginated CD-ROM.

Sandholt, I., K. Rasmussen, and J. Andersen, 2002. A simple interpretation of the surface temperature/vegetation index space for assessment of surface moisture status, *Remote Sensing of Environment*, 79:213–224.

Schmugge, T.J., W.P. Kustas, J.C. Ritchie, T.J. Jackson, and A. Rango, 2002. Remote sensing in hydrology, *Advances in Water Resources*, 25:1367–1385.

Schnur, M.T., H. Xie, and X. Wang, 2010. Estimating root zone soil moisture at distant sites using MODIS NDVI and EVI in a semi-arid region of southwestern USA, *Ecological Informatics*, 5(5):400–409.

Sobrino, J.A., B. Franch, C. Mattar, J.C. Jiménez-Muñoz, and C. Corbari, 2012. A method to estimate soil moisture from Airborne Hyperspectral Scanner (AHS) and ASTER data: Application to SEN2FLEX and SEN3EXP campaigns, *Remote Sensing of Environment*, 117:415–428.

Tang, R., Z.L. Li, and B. Tang, 2010. An application of the Ts-VI triangle method with enhanced edges determination for evapotranspiration estimation from MODIS data in arid and semi-arid regions: Implementation and validation, *Remote Sensing of Environment*, 114:540–551.

Thenkabail, P.S., E.A. Enclona, M.S. Ashton, and B. Van Der Meer, 2004. Accuracy assessments of hyperspectral waveband performance for vegetation analysis applications, *Remote Sensing of Environment,* 91:354–376.

Thenkabail, P.S., G.J. Lyon, and A. Huete, 2011. *Hyperspectral Remote Sensing of Vegetation*, CRC Press/Taylor and Francis Group, Boca Raton, London, New York, 705 p.

Thenkabail, P.S., I. Mariotto, M.K. Gumma, E.M. Middleton, D.R. Landis, and F.K. Huemmrich, 2013. Selection of hyperspectral narrowbands (HNBs) and composition of hyperspectral twoband vegetation Indices (HVIs) for biophysical characterization and discrimination of crop types using field reflectance and Hyperion/EO-1 data, *IEEE Journal of Selected Topics in Applied Earth Observations and Remote Sensing*, 6(2):1–13.

Venturini, V., G. Bisht, S. Islam, and L. Jiang, 2004. Comparison of evaporative fractions estimated from AVHRR and MODIS sensors over South Florida, *Remote Sensing of Environment*, 93:77–86.

Vermote, E.F., D. Tanré, J.L. Deuzé, L. Herman, and J.J. Morcrette, 1997. Second simulation of the satellite signal in the solar spectrum, 6S: An overview, *IEEE Transactions on Geoscience and Remote Sensing*, 35(3):675–686.

Vogelmann, J.E., B.N. Rock, and D.M. Moss, 1993. Red edge spectral measurements from sugar maple leaves, *International Journal of Remote Sensing*, 14(8):1563–1575.

Wang, Q., P. Li, Z. Pu, and X. Chen, 2011. Calibration and validation of salt-resistant hyperspectral indices for estimating soil moisture in arid land, *Journal of Hydrology*, 408:276–285.

Wang, X., H. Xie, H. Guan, and X. Zhou, 2007. Different responses of MODIS-derived NDVI to root-zone soil moisture in semi-arid and humid regions, *Journal of Hydrology*, 340:12–14.

Whiting, M.L., L. Li, and S.L. Ustin, 2004. Predicting water content using Gaussian model on soil spectra, *Remote Sensing of Environment*, 89:535–552.